The effect of inhomogeneous plastic deformation on the ductility and fracture behavior of age hardenable aluminum alloys

Aladar A. Csontos [a,*], Edgar A. Starke [b]

[a] US Nuclear Regulatory Commission, Office of Nuclear Material Safety and Safeguards, Two White Flint North M/S T7F3, 11545 Rockville Pike, Rockville, MD 20852-2738, USA
[b] Department of Materials Science and Engineering, University of Virginia, 116 Engineer's Way, P.O. Box 400745, Charlottesville, VA 22904–4745, USA

Abstract

The role of alloy composition, grain structure, precipitate microstructure, and precipitate dislocation interactions on the plastic deformation characteristics and the resulting fracture behavior of two isotropic Al–Li–Cu–X alloys designated AF/C-458 (1.8 w/o Li) and AF/C-489 (2.1 w/o Li) was examined. Inhomogeneous deformation due to strain localization from the shearing of the δ' (Al$_3$Li), θ' (Al$_2$Cu), and T$_1$ (Al$_2$CuLi) precipitates lead to fine and coarse planar slip for the AF/C-458 and AF/C-489 alloys, respectively. The intensity of this planar slip was predicted through slip intensity calculations using precipitate density measurements, dislocation particle interactions, and grain boundary misorientation-slip continuity statistics. The slip intensity predictions were corroborated through atomic force microscopy (AFM) measured slip height offsets on the polished surface of single aged and 2% plastically strained tensile samples. Our results suggest that the low ductility of AF/C-489 in comparison to AF/C-458 is primarily due to the much larger slip lengths, i.e. grain size, which increased the strain localization and stress concentrations on grain boundaries, thus promoting low-energy intergranular fracture.
© 2004 Published by Elsevier Ltd.

* Corresponding author.

		Form Approved
Report Documentation Page		*Form Approved* *OMB No. 0704-0188*

Public reporting burden for the collection of information is estimated to average 1 hour per response, including the time for reviewing instructions, searching existing data sources, gathering and maintaining the data needed, and completing and reviewing the collection of information. Send comments regarding this burden estimate or any other aspect of this collection of information, including suggestions for reducing this burden, to Washington Headquarters Services, Directorate for Information Operations and Reports, 1215 Jefferson Davis Highway, Suite 1204, Arlington VA 22202-4302. Respondents should be aware that notwithstanding any other provision of law, no person shall be subject to a penalty for failing to comply with a collection of information if it does not display a currently valid OMB control number.

1. REPORT DATE **10 MAR 2004**	2. REPORT TYPE	3. DATES COVERED **00-00-2004 to 00-00-2004**
4. TITLE AND SUBTITLE **The effect of inhomogeneous plastic deformation on the ductility and fracture behavior of age hardenable aluminum alloys**		5a. CONTRACT NUMBER
		5b. GRANT NUMBER
		5c. PROGRAM ELEMENT NUMBER
6. AUTHOR(S)		5d. PROJECT NUMBER
		5e. TASK NUMBER
		5f. WORK UNIT NUMBER
7. PERFORMING ORGANIZATION NAME(S) AND ADDRESS(ES) **University of Virginia,Department of Materials Science and Engineering,116 Engineer's Way,Charlottesville,VA,22904-4745**		8. PERFORMING ORGANIZATION REPORT NUMBER
9. SPONSORING/MONITORING AGENCY NAME(S) AND ADDRESS(ES)		10. SPONSOR/MONITOR'S ACRONYM(S)
		11. SPONSOR/MONITOR'S REPORT NUMBER(S)
12. DISTRIBUTION/AVAILABILITY STATEMENT **Approved for public release; distribution unlimited**		
13. SUPPLEMENTARY NOTES **The original document contains color images.**		
14. ABSTRACT		
15. SUBJECT TERMS		

16. SECURITY CLASSIFICATION OF:			17. LIMITATION OF ABSTRACT	18. NUMBER OF PAGES	19a. NAME OF RESPONSIBLE PERSON
a. REPORT **unclassified**	b. ABSTRACT **unclassified**	c. THIS PAGE **unclassified**		**22**	

Standard Form 298 (Rev. 8-98)
Prescribed by ANSI Std Z39-18

1. Introduction

The aerospace industry is continuously driven to minimize the operational costs of air vehicles especially in these challenging economic times. One of the most effective methods to reduce costs is through weight reduction of the aerospace vehicles and in particular, the aircraft structural materials. For this reason, lightweight age-hardenable Al alloys are still the primary material of choice for aerospace applications. The development of commercial Al–Li–X alloys has been pursued over the last half century to further reduce the density of Al alloys with the added benefit of increasing the alloy's modulus. In fact, the addition of 2 w/o Li reduces the density of Al by 6% and increases the modulus by 12%. Unfortunately, insufficient ductility and toughness, arising from the propensity for planar slip coupled with severe anisotropy, have hindered the widespread implementation of Al–Li–X alloys.

As a result, the US Air Force initiated a program in 1992 to develop an Al–Li alloy containing greater 2 w/o Li that possessed significantly reduced anisotropic properties compared to those currently available. Starke suggested that an intermediate recrystallization anneal be introduced between the rolling stages in order to reduce the sharp textures caused by rolling and thereby decrease the alloy's anisotropy (Hopkins et al., 1996). This process successfully reduced anisotropy from the 20–25% normally observed in commercial Al–Li–Cu–X alloys to less than 10%. The alloy developed on this Air Force program was designated AF/C-489 with a nominal composition of Al–2.7Cu–2.1Li–0.6 Zn–0.3Mn–0.3Mg–0.05Zr (w/o) (Jata et al., 1996). Unfortunately, the elongation at peak strength was lower than the acceptable level of 5% for aerospace applications. As a result of this research, the Air Force and Alcoa developed a derivative of AF/C-489 designated AF/C-458 with the nominal composition of Al–2.7Cu–1.8Li–0.6Zn–0.3Mn–0.3Mg–0.09Zr (w/o). This AF/C-458 variant possessed much higher elongations, more than double the acceptable limit, while also maintaining similar isotropic mechanical properties. The main goal of the investigation described in this paper was to identify the mechanisms associated with the large difference in ductility. The conventional thought at the time was that the higher Li content in the AF/C-489 alloy increased the volume fraction of the shearable δ' (Al$_3$Li) precipitates which resulted in the lower ductility of AF/C-489 as compared to the AF/C-458 alloy.

2. Background

The overall slip and fracture behavior of age-hardenable Al alloys depend greatly on the microstructure and in particular the deformation characteristics of the

strengthening precipitates in the alloy (Martin, 1979). Gliding dislocations can either shear or bypass (loop) the strengthening precipitates during plastic deformation, which leads to inhomogeneous planar slip or homogeneous wavy glide, respectively. Shearable, coherent, and ordered precipitates promote planar slip whereas non-shearable, incoherent, and bypassed precipitates encourage wavy glide (Hornbogen, 1975). Planar slip is considered inhomogeneous plastic deformation that is concentrated on few slip systems as a result of the local work softening on the operative slip plane. This work softening is due to the reduced cross-section of the sheared precipitates, which decreases the strengthening effectiveness on that specific slip plane. Planar slip continues until an obstacle such as a high-angle grain boundary inhibits further dislocation movement and activates adjacent slip systems to accommodate the applied stress. This localized strain can have a deleterious affect on the ductility and fracture behavior of an alloy by promoting premature intergranular failure (Lutjering and Weissmann, 1970; Gregson and Flower, 1985). Wavy glide is considered homogeneous deformation that operates on many slip systems simultaneously and is typically associated with high stacking-fault energy metals and alloys such as pure Al and solid-solution strengthened Al alloys. Even though precipitation hardened Al alloys have relatively high stacking-fault energies, the overall slip and fracture behavior depends more on the precipitate microstructure and grain structure of the alloy.

The precipitate microstructure of age-hardenable Al–Li–Cu–X alloys may contain δ', θ''/θ' (Al_2Cu), and T_1 (Al_2CuLi) particles depending on composition, pre-age thermomechanical processes, and subsequent heat treatment practices. The δ' precipitates maintain a cube–cube crystallographic relationship with the α-Al matrix while the θ''/θ' and T_1 particles precipitate on matrix {0 0 1} and {1 1 1} habit planes, respectively. The Li contents for both AF/C-458 and AF/C-489 alloys are sufficient to precipitate out the spherical, shearable, and coherent δ' particles (Sanders and Starke, 1982). Gable et al. (2001) showed that plastic deformation prior to artificial aging enhanced the competitive precipitation kinetics of the T_1 precipitate, the more potent strengthener, at the expense of weaker θ''/θ' for AF/C-458. Understanding this precipitation behavior is important because previous investigations (Blankenship and Starke, 1992, 1993; Nie et al., 1996; Huang and Ardell, 1988) treated T_1 as hard non-shearable particles as compared to the weaker shearable θ''/θ' particles. However, coarse planar slip has long been associated with these Al–Li–Cu–X alloys that contain both the shearable δ' and the previously assumed unshearable T_1 particles. Howe et al. (1988) and Csontos and Starke (2000), using high-resolution TEM, showed that T_1 could be sheared during deformation when present in Al–Li–Cu–X alloys.

Low ductility resulting from low energy intergranular fracture in high-purity Al–Li alloys has been previously associated with strain localization in the matrix (Sanders and Starke, 1982; Furukawa et al., 1985; Cassada et al., 1986). The strain localization was attributed to the shearing of δ' particles resulting in coarse planar slip and the formation of intense shear bands. These intense shear bands impinged on grain boundaries and caused premature intergranular fracture and low ductility. Therefore, minimizing strain localization during deformation is critical to increasing

the ductility and improving the fracture behavior of Al–Li–Cu–X alloys. The most effective method of reducing strain localization is to minimize the slip length or the distance between concurrent non-sheared events on the active slip plane. The slip length is a key microstructural parameter used in many fracture models to quantify the degree of strain localization (Duva et al., 1988; Blankenship et al., 1993; Sugamata et al., 1993; Jata and Starke, 1986; Roven, 1992; Hornbogen, 1975). For microstructures containing both shearable and non-shearable precipitates, the slip length can be considered the interparticle spacings between the non-shearable precipitates. The role played by non-shearable particles in homogenizing deformation has been established. Previous work on age-hardenable Al alloys (Walsh et al., 1989; Jata and Vasudevan, 1998; Cassada et al., 1986; Blankenship and Starke, 1993) proved that the development of a matrix microstructure containing non-shearable features could improve the ductility of age hardenable Al alloys. For microstructures containing only shearable precipitates, the slip length can be considered the grain size as sub-grain boundaries have been found to be weak obstacles to dislocation motion (Gregson and Flower, 1985; Kuo and Starke, 1985; Miura and Saeki, 1977, 1978, 1980). Investigations by Terlinde and Luetjering (1982), Gysler et al. (1976) and Mendiratta et al. (1976) have shown that grain size varies inversely to the true fracture strain ($L^{-1} \sim e_f$) for alloys with coherent, ordered, and shearable particles similar to δ' in Al–Li–X alloys.

3. Experimental procedures

The Air Force Research Laboratory and Alcoa furnished both the 1.27 cm thick AF/C-489 and the 1.9 cm thick AF/C-458 alloys that were used for these investigations. Both alloy ingots were direct chill cast, stress relieved, homogenized, hot rolled, annealed at 540 °C for 4 h, and then slow cooled before being hot rolled again. This was followed by a solution anneal at 540 °C for 1 h and an immediate water quench followed by a 6% pre-age stretch to promote the T_1 precipitation and naturally aged at room temperature. This T36 temper serves as the "as-received" material from which all aging studies were carried out. For this paper, only data for the longitudinal direction of the alloys is being reported. All aging studies were conducted in forced air furnaces with temperature fluctuations less than ±2 °C followed by immediate water quenching. Tensile samples were machined into dog-bone tensile bars conforming to ASTM E8-93 substandard size regulations and tested utilizing the screw driven Sintech 10/GL MTS system with a crosshead velocity of 3 mm per minute according to ASTM E8 standards. The real-time elongation of each specimen was observed through a digital display via a computer interface with a MTS extensometer across an initial gauge of 25.0 mm.

The grain structure and microstructural aspects were characterized via optical metallography, scanning electron microscopy (SEM), transmission electron microscopy (TEM), differential scanning calorimetry (DSC), orientation imaging microscopy (OIM), and atomic force microscopy (AFM). Optical microscopy samples were mounted in Buehler's Conductomet, metallographically ground and polished

using 0.05 μm colloidal silica, and finally etched with Keller's agent. TEM samples were cut either from the grip section on additional similarly aged material for micro-structural analysis while samples cut from the gauge section were utilized for slip behavior examinations. The cut wafers were mechanically thinned to ∼150 μm thick, punched into 3 mm disks, and electropolished in a Tenupol twinjet electro polisher at 11 V for the AF/C-458 alloy and 8 V for the AF/C-489 alloy at a flow rate of 3 and photosensitivity of 9. A 7:2 methanol: nitric acid solution chilled to −25 °C was used as the electrolyte.

Digital SEM fractographs were acquired through the use of a DSM982 Gemini field emission SEM operating at 10 kV equipped with dual secondary backscatter electron detectors. OIM data acquisition was performed on a Leo 1550 SEM equipped with a Schottky field-emission gun operating at 20 kV and collected using the OIM DC software package provided by TSL, Inc. To obtain the OIM data, the specimens were tilted 70° toward the camera used to acquire the electron backscatter diffraction patterns (EBSD). Conventional TEM was accomplished using a JEOL 2000FX TEM at 200 kV while high resolution TEM was completed with the JEOL 4000 HREM operating at 400 kV. Weak-beam dark-field (WBDF), centered dark-field (CDF), and bright-field (BF) TEM techniques were used to identify the various precipitate types, dimensions, and distribution. Stereological quantification of the spherical δ', T_1 plates, and θ''/θ' plate shaped precipitates in thin TEM foils was completed using a statistical analysis to overcome thin foil effects which underestimates the diameters and volume fractions of the particles from two-dimensional TEM micrographs. Foil thickness was determined by the convergent-beam method and the dislocation particle interactions were observed using the WBDF technique. AFM samples were polished to 0.05 μm using colloidal silica and then plastically strained to 2% at a strain rate of 1 mm per minute. These polished and strained tensile bars were then examined utilizing a Digital Instruments Dimension 3100 Nano-scope III AFM with 10 nm resolution carbon nanotube tips in the intermittent contact mode.

4. Results and discussion

4.1. As-received T36 grain and sub-grain structure

The grain and sub-grain structures of both as-received T36 unrecrystallized AF/C-458 and AF/C-489 plates have been detailed elsewhere (Csontos and Starke, 2000, in press). Table 1 summarizes these results for both as-received unrecrystallized T36 plates and indicates that both have similar sub-grain structures with very different grain structures. The number of grains counted in an optical micrograph over a 500 mm circumference was up to 3 times greater in AF/C-458 than AF/C-489. This indicates that the AF/C-489 plate contained a much larger average grain size in all three planes, i.e. rolling (LT), longitudinal (LS), and short transverse (ST), as compared to AF/C-458. AF/C-458 grains also possessed an aspect ratio roughly twice that of AF/C-489, which indicates a more pancaked grain structure for AF/C-458.

Table 1
As-received T36 unrecrystallized plate grain structures

Plate thickness	Sub-grain size (μm)	# Grains/500 mm			Aspect ratio		
		LT	LS	ST	LT	LS	ST
AF/C-458							
0.50″	∼5–10	42.2	228.5	261.3	6.7	34.2	24.6
AF/C-489							
0.75″	∼5–10	18.0	75.0	83.0	3.4	19.7	10.1

Conversely, the substructure of both alloys was relatively similar with sub-grain sizes on the order of 5–10 μm in diameter.

4.2. Microstructure, precipitation response, and mechanical properties

The precipitation response for both alloys was determined through DSC and TEM studies from the T36 as-received temper. We found that the θ' and T_1 precipitation onset temperatures were between 90–95 and 120–125 °C, respectively, for both alloys. We were then able to determine the effect of T_1 aging kinetics on the strength of various single aged routes above 120 °C through Rockwell hardness measurements. These results indicate that the 150 °C single age practice provides a good combination of both high matrix T_1 nucleation and growth rates, i.e. near the nose of the time–temperature-transformation curve. Next, we obtained the baseline 150 °C tensile data as a function of aging time for the AF/C-458 longitudinal direction as seen in Fig. 1. Note that the best combination of strength to ductility was in the slightly underaged condition at 150 °C for 24 h and that the data did not change much between 24 h and 2 weeks showing that significant overaging did not occur for up to 2 weeks at 150 °C. This single age 150 °C for 24 h was used for our baseline mechanical properties for both alloys because temperatures greater than 150 °C have been shown to precipitate the deleterious T_2 ($Al_6Cu(LiMg)_3$) embrittling phase (Lewis et al., 1987) and coarse grain boundary T_1 with corresponding precipitate free zones (Roven, 1992) in age-hardenable Al–Li–Cu–X alloys.

The precipitate microstructure of the baseline 150 °C 24 h single age for alloys AF/C-458 and AF/C-489 are shown in Figs. 2 and 3, respectively. The BF and CDF TEM micrographs clearly show T_1 and δ' as the major strengthening precipitates in both alloys with some θ' engloved with δ' for this 150 °C 24 h single age condition. Matrix T_1 precipitation is high due to the introduction of matrix dislocations arising from the 6% pre-age stretch in both alloys with some fine grain boundary T_1 particles. Although these fine grain boundary T_1 variants were found in both alloys, deleterious coarse grain boundary δ (AlLi), θ (Al_2Cu), T_2, T_B (Al_7Cu_4Li), R (Al_5Cu-Li_3), and I (Al_6CuLi_3) (Hardy and Silcock, 1959) with their associated precipitate free zones were not found in either alloy for this 150 °C 24 h age. Nevertheless, minimizing the observed grain boundary T_1 precipitation is important in order to determine whether the grain boundary T_1 contributed to the low ductility in the AF/C-489 alloy. Since grain and sub-grain boundary T_1 were observed in both 150 °C 24 h aged
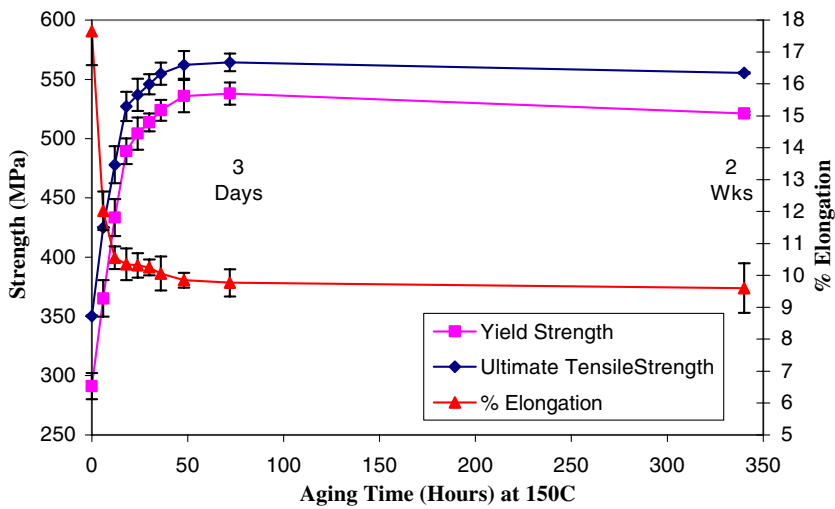
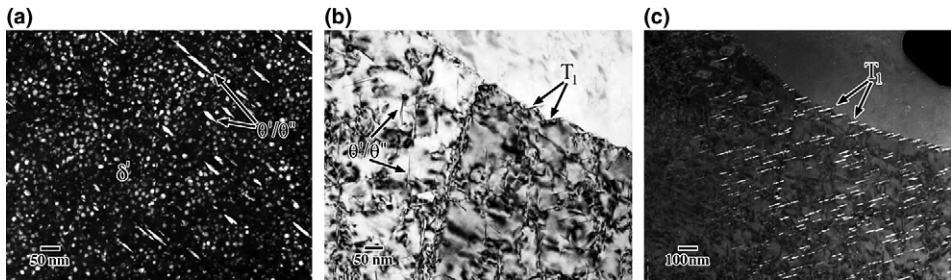Fig. 1. Longitudinal tensile properties as a function of aging at 150 °C.

Fig. 2. AF/C-458 150 °C 24 h micrographs (a) CDF image showing δ' and θ'/θ'' engloved with δ', $b = [0\ 1\ 1]_\alpha\ g = (1\ 0\ 0)_{\delta'}$, (b) BF indicating θ'/θ'' and matrix and grain boundary puckering T_1, $b = [1\ 1\ 0]_\alpha$, (c) CDF micrograph showing matrix and grain boundary puckering T_1, $b = [1\ 1\ 0]_\alpha\ g = \frac{1}{2}(1\ 1\ 1)_\alpha$.

Fig. 3. AF/C-489 150 °C 24 h micrographs (a) CDF image showing δ' and θ'/θ'' engloved with δ', $b = [0\ 1\ 1]_\alpha\ g = (1\ 0\ 0)_{\delta'}$, (b) BF indicating θ'/θ'' and matrix and grain boundary puckering T_1, $b = [1\ 1\ 0]_\alpha$, (c) CDF micrograph showing matrix and grain boundary puckering T_1, $b = [1\ 1\ 0]_\alpha\ g = \frac{1}{2}(1\ 1\ 1)_\alpha$.
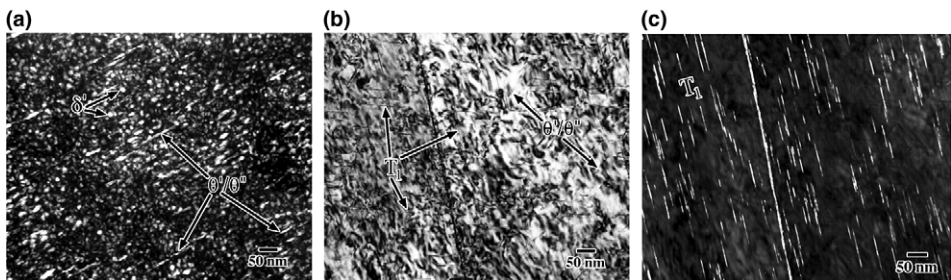
alloys, duplex aging studies were conducted in an effort to minimize grain and sub-grain boundary T_1 and maximize matrix T_1 precipitation.

A pre-age stretch coupled with a low/high temperature duplex aging schedule has been shown to substantially increase the ductility and fracture toughness of various Al–Li alloys (Ashton et al., 1986; Ahrens and Starke, 1989; Blankenship and Starke, 1992, 1994). The experimentally determined T_1 solvus boundary was measured to be between 120 and 125 °C for both alloys. The low temperature age above 120 °C was designed to maximize the driving force for matrix T_1 nucleation followed by a higher temperature age to promote subsequent matrix T_1 growth. Other duplex aging studies with low temperature agings between 100 and 120 °C were designed to precipitate a very fine dispersion of θ' to either tie up the Cu solute in the matrix or provide possible nucleation sites for matrix T_1 precipitation on the θ' particles (Noble and Thompson, 1972) during subsequent higher temperature aging. By either method, the design of these aging routes was to increase the matrix T_1 precipitation kinetics, thus, minimizing the availability of solute to form the grain boundary precipitates. Furthermore, these low/high aging studies were also designed to increase the matrix T_1 number density, thereby, reducing the T_1 interparticle spacing, which would act to decrease the effective slip length, if T_1 is unshearable, and hopefully promote greater ductility.

The overall results of the duplex aging practices in comparison to the 150 °C 24 h age for both AF/C-458 and AF/C-489 alloys are shown in Tables 2 and 3 for the longitudinal and long transverse directions, respectively. These results indicate that no significant changes occurred to the tensile properties of duplex aged AF/C-458, suggesting a large processing window. Significant improvements were made though by employing the duplex aging schedules for AF/C-489 as the ductility increased by as much as 65% with a decrease of only 4% and 2% for the longitudinal yield and

Table 2
Longitudinal tensile mechanical properties of T86 single and double aged AF/C-458 and AF/C-489

Aging standard	YS (MPa)	Standard deviation	UTS (MPa)	Standard deviation	Elongation (%)	Standard deviation
150 °C 24 h						
AF/C-458	504.3	13.6	537.0	13.6	10.3	0.4
AF/C-489	512.9	8.2	554.8	3.1	4.9	1.0
100 °C 24 h and 150 °C 24 h						
AF/C-458	500.8	8.7	541.4	11.5	10.6	0.4
AF/C-489	474.4	11.6	533.1	3.7	7.3	0.8
120 °C 18 h and 150 °C 24 h						
AF/C-458	500.4	13.7	543.4	13.5	10.8	0.3
120 °C 48 h and 150 °C 22 h						
AF/C-489	491.7	17.9	544.8	7.3	8.1	0.7
130 °C 24 h and 150 °C 23 h						
AF/C-458	495.3	9.8	539.0	17.3	10.8	0.8
AF/C-489	495.7	17.2	548.7	10.0	7.9	0.6

Table 3
Long transverse tensile mechanical properties of T86 single and double aged AF/C-458 and AF/C-489

Aging standard	YS (MPa)	Standard deviation	UTS (MPa)	Standard deviation	Elongation (%)	Standard deviation
150 °C 24 h						
AF/C-458	510.5	19.6	538.2	5.7	10.4	0.8
AF/C-489	468.7	4.3	529.9	2.0	3.6	1.1
100 °C 24 h and 150 °C 24 h						
AF/C-458	501.1	11.5	539.5	14.8	10.5	1.1
AF/C-489	414.8	2.4	508.1	1.2	5.0	0.3
120 °C 18 h and 150 °C 24 h						
AF/C-458	502.2	2.0	551.5	1.7	10.5	0.2
120 °C 48 h and 150 °C 22 h						
AF/C-489	430.0	13.8	524.0	10.1	6.2	0.6
130 °C 24 h and 150 °C 23 h						
AF/C-458	515.4	14.7	551.5	13.4	10.7	1.1
AF/C-489	435.4	20.8	526.7	21.1	5.6	0.2

ultimate tensile strengths, respectively. This result was also observed for the long transverse direction with a 72% increase in ductility with a decrease of only 8% and 1% for the yield and ultimate tensile strengths, respectively. Nevertheless, we found that all of our investigated single and double aged samples contained fine grain boundary T_1 with no coarse grain boundary T_1, T_2, or precipitate free zones. Hence, we determined that the fine grain boundary T_1 was not the primary cause for the low ductility of AF/C-489.

Table 4
Quantitative T_1 precipitate measurements and standard deviations for single and duplex aged AF/C-458 and AF/C-489 alloys corresponding to the mechanical properties in Tables 2 and 3

Alloy/aging practice	T_1 vol%	Standard deviation	T_1 # density #/(μm^{-3})	Standard deviation	T_1 mean diameter (nm)	Standard deviation
AF/C-458						
150 °C 24 h	3.0%	0.12	7650	696.5	57	2.8
100 °C 24 h						
150 °C 24 h	3.0%	0.08	9380	739.8	51	1.3
120 °C 18 h						
150 °C 24 h	2.9%	0.05	10,970	703.0	47	0.6
130 °C 24 h						
150 °C 23 h	2.9%	0.07	11,870	298.4	44	1.1
AF/C-489						
150 °C 24 h	3.0%	0.10	7620	890.9	56	2.9
100 °C 24 h						
150 °C 24 h	1.3%	0.05	5550	363.9	43	0.5
120 °C 48 h						
150 °C 22 h	1.8%	0.11	7710	146.1	42	1.8
130 °C 24 h						
150 °C 23 h	1.8%	0.18	7660	825.6	42	0.6

The mechanical response of both alloys to the duplex aging treatments can be related to their corresponding precipitate microstructure. Quantitative TEM results in Tables 4–6 demonstrate that no significant changes in θ', T_1, or δ' volume fractions were found for the single and duplex aged AF/C-458 alloy although the number density increased and precipitate diameters decreased with the double age. The

Table 5

Quantitative θ' precipitate measurements and standard deviations for single and duplex aged AF/C-458 and AF/C-489 alloys corresponding to the mechanical properties in Tables 2 and 3

Alloy/aging practice	θ' vol%	Standard deviation	θ' # density #/(μm^{-3})	Standard deviation	θ' mean diameter (nm)	Standard deviation
AF/C-458						
150 °C 24 h 100 °C 24 h	0.3%	0.05	1440	237.5	48	0.9
150 °C 24 h 120 °C 18 h	0.3%	0.03	10,330	24.5	19	1.0
150 °C 24 h 130 °C 24 h	0.3%	0.02	11,220	631.3	17	0.4
150 °C 23 h	0.4%	0.01	10,180	495.4	22	0.7
AF/C-489						
150 °C 24 h 100 °C 24 h	0.3%	0.01	4610	453.6	29	0.8
150 °C 24 h 120 °C 48 h	1.7%	0.13	75,860	3616.9	17	0.3
150 °C 22 h 130 °C 24 h	1.1%	0.03	28,640	3215.6	22	0.1
150 °C 23 h	1.1%	0.01	29,500	2544.3	22	1.0

Table 6

Quantitative δ' precipitate measurements and standard deviations for single and duplex aged AF/C-458 and AF/C-489 alloys corresponding to the mechanical properties in Tables 2 and 3

Alloy/aging practice	δ' vol%	Standard deviation	δ' mean diameter (nm)	Standard deviation
AF/C-458				
150 °C 24 h 100 °C 24 h	12.6%	0.42	15.8	0.11
150 °C 24 h 120 °C 18 h	12.6%	0.35	15.4	0.11
150 °C 24 h 130 °C 24 h	12.5%	0.35	15.6	0.11
150 °C 23 h	12.7%	0.28	15.3	0.05
AF/C-489				
150 °C 24 h 100 °C 24 h	17.3%	0.33	16.0	0.14
150 °C 24 h 120 °C 48 h	19.2%	0.64	15.1	0.06
150 °C 22 h 130 °C 24 h	18.5%	0.21	15.7	0.11
150 °C 23 h	18.3%	0.35	15.8	0.13

precipitation response between single and duplex aged AF/C-489, on the other hand, was significantly different. The duplex age competitively precipitated much more θ' at the expense of T_1 with relatively similar δ' volume fractions. The shearable δ' volume fraction was found to be on average ∼5–6.5% greater in the T86 aged AF/C-489 alloy as compared to similarly aged AF/C-458 alloys. From this data, the increased ductility and slightly lower yield strengths of the duplex aged AF/C-489 alloy is attributed to the extensive precipitate microstructure refinement, i.e. reduced inter-particle spacings and the competitive precipitation of a much greater number density of the weaker θ' plates at the expense of stronger T_1 particles with relatively similar δ' volume fractions.

4.3. Slip and fracture behavior analysis

Matrix T_1 precipitates were previously treated as unshearable particles that strengthen via the Orowan bypassing mechanism. However, our TEM and HREM micrographs in Figs. 4 and 5 conclusively show that T_1 shears in both T86 alloys aged at 150 °C 24 h resulting in shear band formation. TEM investigations for all aging practices showed the formation of these intense shear bands indicating that matrix T_1 sheared in all of the duplex aged conditions as well. TEM and OIM data showed that the resultant intense shear bands in all aged alloys easily traversed low-angle sub-grain boundaries while high-angle grain boundaries with greater that 11° misorientation for T86 AF/C-458 and 11–18° misorientation for T86 AF/C-489 arrested slip. The optical microscopy images in Figs. 6 and 7 reveal the macroscopic nature of planar slip resulting from the shearing of δ', θ', and T_1 precipitates in both 2% plastically strained 150 °C 24 h aged alloys. The first set of micrographs in Fig. 6 was acquired from aged and 2% plastically strained tensile bars that were then polished and etched with Keller's agent to bring out the slip character. To discount the preferential effects of etching that could skew the results, the optical samples in Fig. 7 were first aged then polished down with colloidal silica with no etching and finally stretched to 2% plastic strain. From these micrographs, we can clearly see a qualitative difference in the planar slip intensities between the alloys. The AF/C-489 micrographs clearly show a much greater amount of planar slip as compared to the AF/C-458 alloy, which could partially explain the lower ductility of AF/C-489.

The fracture behavior of the single and duplex aged alloys is shown in the SEM fractographs in Fig. 8. The fractographs show the differences in fracture behavior between the AF/C-458 and AF/C-489 alloys. The fracture behavior for all single and duplex aged AF/C-458 longitudinal tensile samples remained fairly consistent with the aforementioned mechanical and precipitation behavior. Transgranular, slanted 45° fracture paths were typical for AF/C-458 and the fracture surfaces indicate a large amount of high-energy transgranular shearing, grain boundary sliding, dimpled rupture, and microvoid coalescence (MVC) with a minimum of intergranular fracture. In contrast to AF/C-458, the AF/C-489 single aged 150 °C 24 h fracture paths were predominantly flat with large areas of coarse intergranular fracture sites evident. These intergranular fracture sites also suggested that coarse planar slip promoted the low-energy intergranular fracture because slip offsets ∼200 nm in height
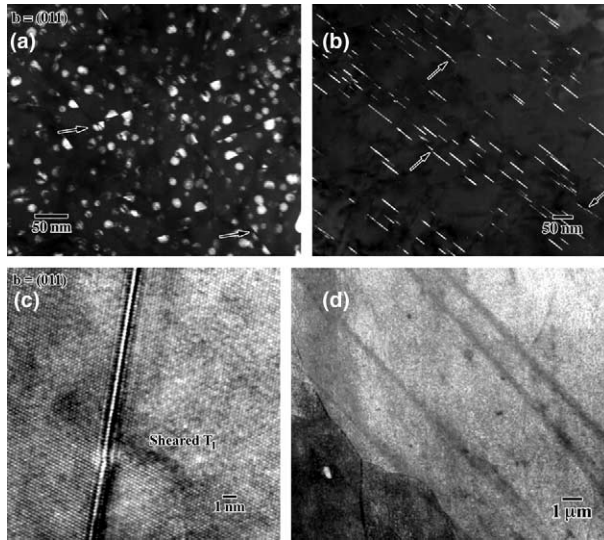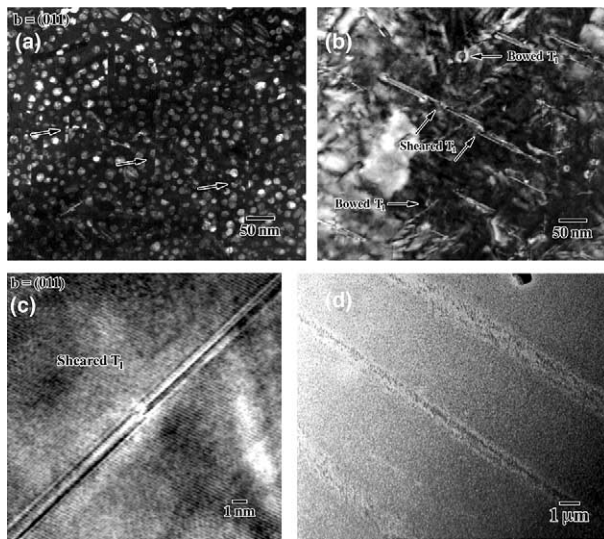
Fig. 4. AF/C-458 150 °C 24 h 2% plastic strained micrographs (a) CDF image showing sheared δ' (arrows), $b = [1\,1\,0]_\alpha$ $g = (1\,0\,0)_{\delta'}$, (b) CDF indicating sheared T_1, $b = [1\,1\,0]_\alpha$ $g = \frac{1}{2}(1\,1\,1)_\alpha$, (c) HREM micrograph showing sheared T_1, $b = [1\,1\,0]_\alpha$, (d) BF image showing shear bands along $(1\,1\,1)_\alpha$ trace, $b = [1\,1\,0]_\alpha$.
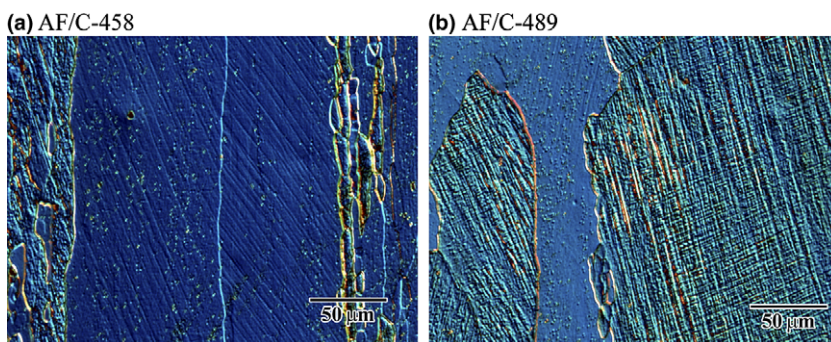

Fig. 5. AF/C-489 150 °C 24 h 2% plastic strained micrographs (a) CDF image showing sheared δ' (arrows), $b = [1\,1\,0]_\alpha$ $g = (1\,0\,0)_{\delta'}$, (b) WBDF indicating sheared and bowed T_1, $b = [1\,1\,0]_\alpha$, $g, 3g = \frac{1}{2}(1\,\bar{1}\,1)_\alpha$, (c) HREM micrograph showing sheared T_1, $b = [1\,1\,0]_\alpha$, (d) BF image showing shear bands along $(1\,1\,1)_\alpha$ trace, $b = [1\,1\,0]_\alpha$.

Fig. 6. Optical micrographs of 2% plastically strained and then polished and etched T86 150 °C 24 h single aged (a) AF/C-458 and (b) AF/C-489 samples that qualitatively indicate greater planar slip intensity for AF/C-489.
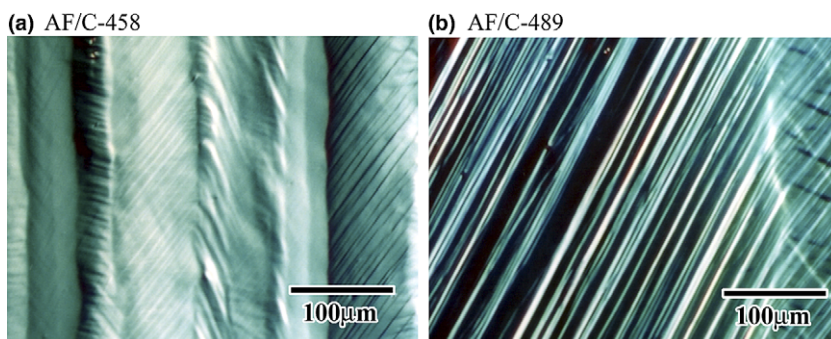

Fig. 7. Optical micrographs of T86 150 °C 24 h aged samples that were polished and 2% plastically strained for (a) AF/C-458 and (b) AF/C-489 that qualitatively indicate greater slip intensity for AF/C-489 as larger planar surface offsets.

were evident on the fracture surface. This fracture behavior is not found in any of the duplex aged tensile samples which fractured close to 45° indicating more high energy transgranular shearing, which is favorable for high ductility. However, some regions of low-energy intergranular fractured grains were still evident along with smaller areas of transgranular shearing and MVC.

To further clarify the effect of planar slip on fracture behavior, the quantitative planar slip intensities were measured for both alloys in the single aged 150 °C 24 h T86 condition and compared to the previous qualitative optical microscopy results. An AFM with a 10 nm vertical resolution was employed to accurately measure the planar slip offsets observed on the surface of aged, polished, and 2% plastically strained AF/C-458 and AF/C-489 samples with no etch. The results of this investigation are shown in Figs. 9 and 10. Fig. 9 demonstrates the method used to measure the slip offsets as statistically represented in Fig. 10 as well as the three-dimensional representation of the slip offsets for both T86 alloys. This technique measures the
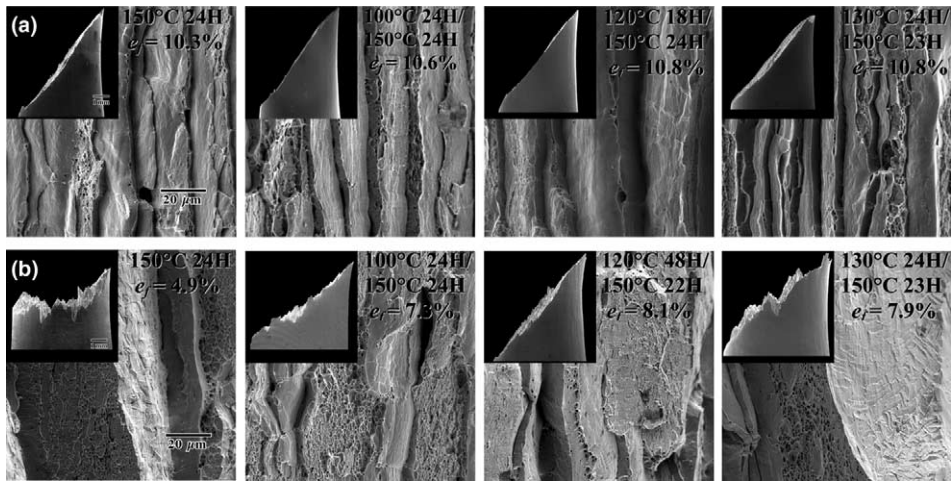
Fig. 8. SEM fractographs of single and duplex aged T86 (a) AF/C-458 and (b) AF/C-489.

intensity of the planar slip as the height of the slip offset associated with dislocations that have egressed to the surface of the polished flat sample during the 2% plastic strain. These three-dimensional AFM images coupled with the measured slip offset statistical data in Fig. 10 clearly demonstrate the strong planar slip characteristics and much larger slip offsets in AF/C-489 versus AF/C-458. These measurements corroborate the previous observations made in Figs. 6 and 7, which illustrate the much higher planar slip intensities for AF/C-489 as compared to AF/C-458.

4.4. Strain localization quantification

To quantify the amount of strain localization in both alloys and relate it to their differences in ductility, a methodology was developed to calculate the amount of planar slip impinging at high-angle grain boundaries. These strain localization results were then correlated to our previous AFM microscopy experiment to corroborate the calculations. From this data, we were able to quantitatively describe this stress concentration at the tip of a dislocation pile-up impinging upon a deformation barrier as the shear stress concentration, τ_c, which is N (number of dislocations) times the resolved shear stress, τ_{rss}:

$$\tau_c = N\tau_{rss}. \tag{1}$$

Shearing of a strong precipitate like T_1 or nucleating a crack at a grain boundary can then proceed when the localized shear stress intensities exceed a critical shear stress, τ_c^*. The slip intensity could then be quantified as the number of dislocations expected in a pileup at a high-angle grain boundary, which is related to the order hardening and shearing characteristics of the δ' precipitates and the slip length of the alloy through the relationship (Duva et al., 1988):
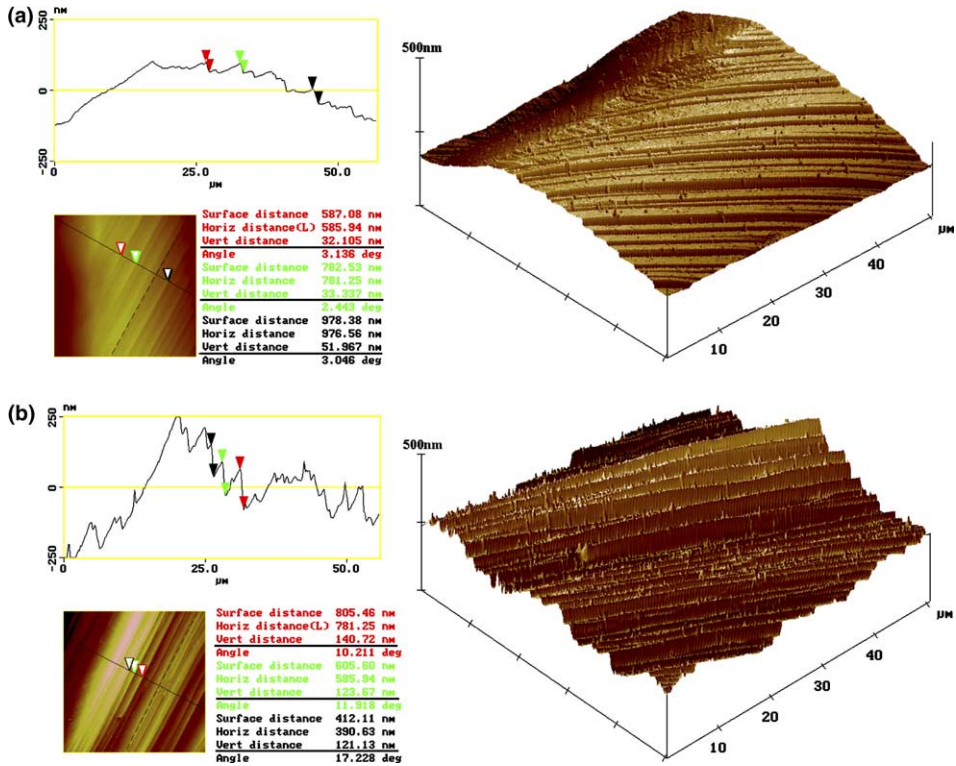
Fig. 9. AFM images of slip offsets from polished and 2% $\varepsilon_{plastic}$ 150 °C 24 h aged T86 (a) AF/C-458 and (b) AF/C-489 samples.

$$N = f_v^{1/2} r_p^{1/2} L \frac{C_p}{C_B b},$$
(2)

where N is the number of dislocations in a pileup, f_v = δ' volume fraction, r_p = δ' radius, L, the slip length, $C_p = (\gamma^{3/2}/2b)(3/\pi G b^2)^{1/2}$ where γ is the antiphase domain boundary energy of δ', b the Burgers vector and G the shear modulus of the matrix, and $C_B = G/\pi(1 - v)$ where v is Poisson's ratio.

In an effort to calculate the amount of strain localization impinging on a typical grain boundary, only the average slip length for both alloys was needed. Previous TEM micrographs showed that T_1 sheared and sub-grain boundaries did not arrest slip, which suggests that the average T_1 interparticle spacing or sub-grain size could not be considered the slip length for these alloys. We also showed that grain boundaries with misorientation angles equal to or greater than 11° and 11–18° for AF/C-458 and AF/C-489, respectively, arrested slip. Consequently, OIM investigations from the LS and ST planes were conducted to measure the slip length, i.e. the average distance between concurrent grain boundaries with 11° and 11–18° misorientations. This procedure is schematically shown in Figs. 10–12 where the distance was
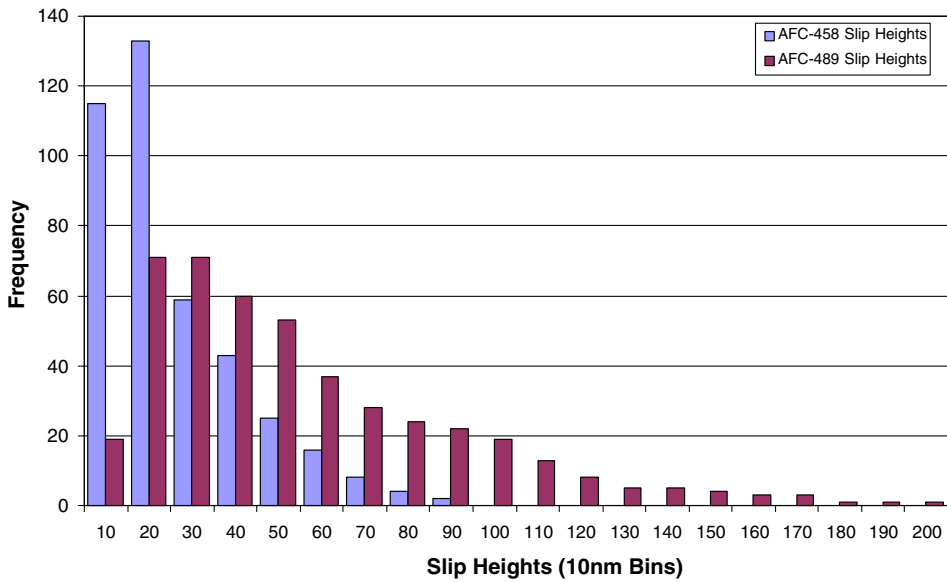
Fig. 10. Statistical results of the measured AFM slip offsets for the T86 150 °C 24 h aged 2% $\varepsilon_{plastic}$ AF/C-458 and AF/C489 alloys.

measured at a 45° angle, i.e. corner to corner, so as to discount for any skewing of the data due to the elongated grain structure. The OIM simulated micrographs qualitatively demonstrate the large slip length differences between the AF/C-458 and AF/C-489 alloys by denoting the 11° and 18° misoriented grain boundaries in yellow and black, respectively. The misorientation profiles and inverse pole figure maps clearly show the much larger slip lengths measured for the AF/C-489 alloy as compared to the finer grained AF/C-458 alloy. In fact, the measured slip lengths for the AF/C-489 alloy were on average ~3 times greater than similarly examined planes and misorientations of the AF/C-458 alloy (see Fig. 12).

Table 7 shows the results of these planar slip intensity calculations with the OIM measured slip lengths. The calculations conclusively show that planar slip intensities are on average 3–3.5 times greater in the AF/C-489 alloy when compared to the AF/C-458 alloy for all measured slip lengths with misorientations greater than 5°, 11°, and 18° except for the sub-grains. The calculations for the sub-grains in both alloys were conducted so as to exclusively distinguish the role that δ' plays in strain localization and ductility, i.e. keeping the slip length constant at 5 μm which is approximately the average sub-grain size for both unrecrystallized alloys. These calculations indicate that the increased δ' volume fraction in the AF/C-489 alloy only contributed approximately 4 more dislocations to the pileup when compared to the AF/C-458 alloy. Hence, the Duva model shows that the number of dislocations in a pileup varies directly with slip length and to a lesser extent on the square root of δ' volume fraction for this alloy, i.e. the higher δ' volume fraction in the T86 AF/C-489 alloy
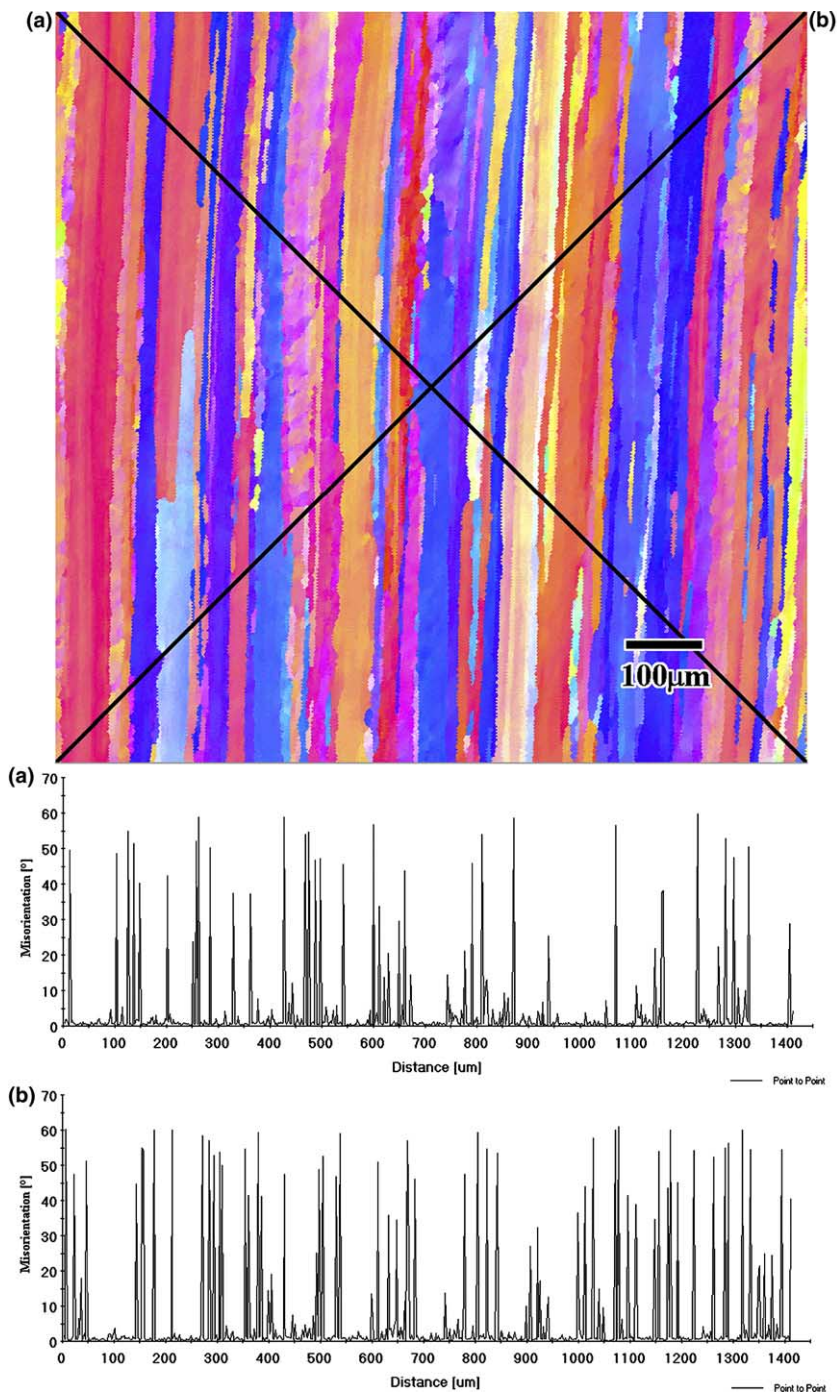
Fig. 11. OIM determined grain boundary misorientation profiles of the LS plane from the as-received T36 AF/C-458 alloy.
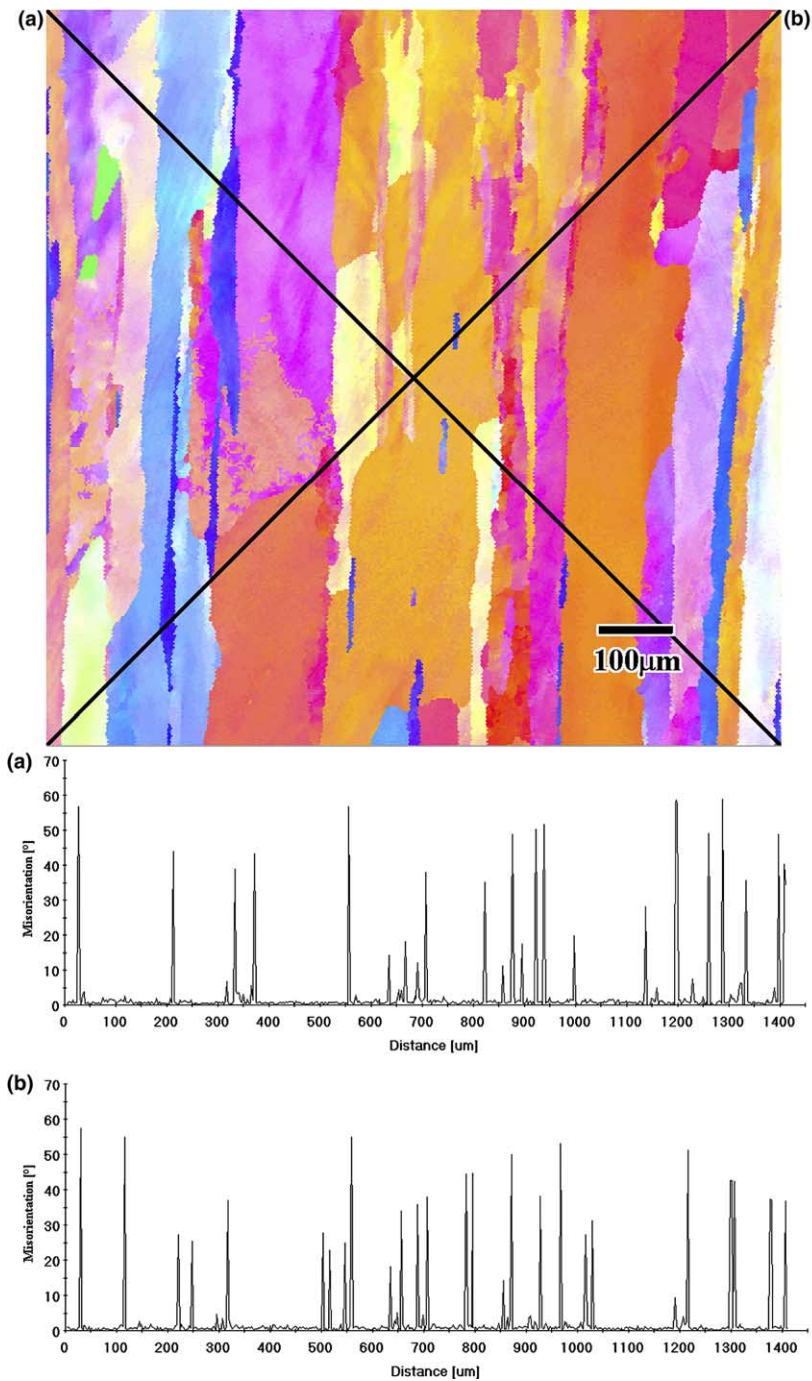
Fig. 12. OIM determined grain boundary misorientation profiles of the LS plane from the as-received T36 AF/C-489 alloy.

Table 7
Results and correlation of slip intensity calculations and physically measured AFM slip offsets for 150 °C 24 h aged AF/C-458 and AF/C-489

	Subgrains	>5° misorientation	>11° misorientation	>18° misorientation	AFM slip height (nm)
AF/C-458 alloy aged 150 °C 24 h					
delta′ average radius (nm)	7.9	7.9	7.9	7.9	–
δ' volume fraction	0.126	0.126	0.126	0.126	–
C_P/C_Bb (m$^{-1.5}$)	3.35E+11	3.35E+11	3.35E+11	3.35E+11	–
SL plane					
Slip length (μm)	~5.0	13.26	21.03	25.43	–
Standard deviation	–	0.95	2.66	3.78	–
# of dislocations (N)	52.8	147.2	235.7	278.0	–
Slip height Nb (nm)	15.1	42.1	67.4	79.5	<83.7
AF/C-489 alloy aged 150 °C 24 h					
δ' average radius (nm)	8.0	8.0	8.0	8.0	–
δ' volume fraction	0.173	0.173	0.173	0.173	–
C_P/C_Bb (m$^{-1.5}$)	3.35E+11	3.35E+11	3.35E+11	3.35E+11	–
SL plane					
Slip length (μm)	~5.0	42.55	69.93	85.69	–
Standard deviation	–	11.26	18.23	8.35	–
# of dislocations (N)	62.0	527.4	866.7	1062.1	–
Slip height Nb (nm)	17.7	150.8	247.9	303.8	<195.8

increases the slip intensity by approximately 15% while the difference in slip length increases the intensity by as much as ~350%. This ~15% can also be negated by reducing the slip length of AF/C-489 through grain refinement even further than found in AF/C-458. Thus, the Duva model and AFM results suggests that the major cause for the greater planar slip intensities and lower ductility in AF/C-489 is due to the ~3 times greater average slip lengths as compared to the finer grained AF/C-458 alloy.

Nevertheless, the Duva model was unable to predict the increased ductility of the AF/C-489 alloy by duplex aging because it was unable to predict the effect that microstructural refinement and the variation in the competitive precipitation have on slip intensity when all of the precipitates shear during plastic deformation, i.e. when the slip length is greater than the average interparticle spacing of shearable precipitates. The development of a modified Duva equation that accounts for the microstructure when all of the precipitates shear (and for different types of precipitates) during plastic deformation is underway. We attribute the increased ductility and slightly lower yield strengths of the duplex aged AF/C-489 alloy to the substantial refinement in the precipitate microstructure (interparticle spacings) and the competitive precipitation of a high number density of the weaker θ' plates at the expense of stronger T_1 particles with relatively similar δ' volume fractions.

By going through the calculations for both alloys, the Duva model predicts that AF/C-489 experienced between 2 and 4 times greater slip concentrations than

AF/C-458. The AFM technique confirmed these predictions by showing remarkably similar results and that the planar slip offsets on the surface of polished and stretched AF/C-489 samples were more than double that found for the AF/C-458 alloy. The much larger slip lengths for the AF/C-489 alloy greatly increased the intensity of planar slip impinging upon a grain boundary, thereby, promoting low-energy intergranular fracture and low ductility. Therefore, our results suggest the low ductility of the AF/C-489 alloy is not intrinsically related to the higher (2.05 wt%) Li content, but due primarily to the much larger slip lengths as represented by the $\sim$3 times larger grain size as compared to the AF/C-458 alloy.

5. Conclusions

1. In summary, our results indicate that the low ductility of AF/C-489 in comparison to AF/C-458 is primarily due to the $\sim$3 times greater slip length and to a much lesser extent on the increased volume fraction of shearable δ'. The much larger slip lengths greatly increased the intensity of planar slip impinging upon a grain boundary. Slip intensity modeling suggests AF/C-489 ($\varepsilon_f = 4.9\%$) experiences $\sim$2–4 times greater stress concentrations at the grain boundary as compared to AF/C-458 ($\varepsilon_f = 10.3\%$). This results in earlier fracture and lower ductility for AF/C-489. Therefore, our results suggest the low ductility of AF/C-489 is not intrinsically related to the higher 0.3 w/o Li, but primarily due to the larger slip lengths associated with the larger grain size.
2. Duplex aging treatments for the AF/C-489 alloy resulted in significant increases in ductility by as much as 65% with only a small decrease of 4% and less than 2% for the yield and ultimate tensile strengths, respectively. The increased ductility and slightly lower yield strengths of the duplex aged AF/C-489 alloy is attributed to the large precipitate microstructure refinement, i.e. reduced interparticle spacings, and the competitive precipitation of a high number density of the weaker θ' plates at the expense of stronger T_1 particles with relatively similar δ' volume fractions.
3. In contrast, no significant strength and ductility improvements were found through duplex aging practices for the AF/C-458 alloy due to the similar precipitation behaviors for the single and duplex ages.
4. Both δ' and T_1 were found to shear which lead to the formation of intense shear bands indicating strain localization in all single and duplex aged samples.
5. Grain boundary T_1 was found in all aged conditions for this study, but was not considered to be the major cause for the lower ductility of AF/C-489.
6. Slip easily traversed low-angle sub-grain boundaries while slip was arrested by high-angle grain boundaries greater than or equal to 11° for AF/C-458 and between 11° and 18° for AF/C-489.
7. Fractography of the T86 AF/C-489 alloy indicated more classic low-energy intergranular fracture regions with $\sim$200 nm slip offsets than the T86 AF/C-458 alloy which demonstrated ductile fracture via high energy transgranular shearing, grain boundary sliding, dimpled rupture, and MVC.

Acknowledgement

References

Ahrens, T., Starke Jr., E.A., 1989. Effect of stretch on grain boundary precipitation in 8090. In: Sanders, T.H. Jr.Jr., Starke, E.A. Jr.Jr. (Eds.), Al–Li Alloys V. MCE Publications Ltd, Birmingham, UK, p. 385.

Ashton, R.F., Thompson, D.S., Starke Jr., E.A., Lin, F.S., 1986. Processing Al–Li–Cu–(Mg) alloys. In: Baker, C., Gregson, P.J., Harris, S.J., Peel, C.H. (Eds.), Al–Li Alloys III. The Institute of Metals, London, England, p. 66.

Blankenship Jr., C.P., Starke Jr., E.A., 1992. Improved toughness in Al–Li–Cu–Mg–Ag–Zr alloy X2095. Scripta Metall. 26, 1719.

Blankenship, C.P., Starke Jr., E.A., 1993. Mechanical behavior of double-aged AA8090. Metall. Trans. A 24A, 833.

Blankenship Jr., C.P., Starke Jr., E.A., 1994. Structure–property relationships in Al–Li–Cu–Mg–Ag–Zr alloy X2095. Acta Metall. 42, 845.

Blankenship Jr., C.P., Hornbogen, E., Starke Jr., E.A., 1993. Predicting slip behavior in alloys containing shearable and strong particles. Mater. Sci. Eng. A169, 33.

Cassada, W.A., Shiflet, G.J., Starke Jr., E.A., 1986. The effect of germanium on the precipitation and deformation behavior of Al–2Li alloys. Acta Metall. 34, 367.

Csontos, A.A., Starke Jr., E.A., 2000. The effect of processing and microstructure development on the slip and fracture behavior of the 2.1 w/o Li AF/C-489 and 1.8 w/o Li AF/C-458 Al–Li–Cu–X alloys. Metallurgical and Materials Transactions A 31 (8), 1965–1976.

Csontos, A.A., Starke Jr., E.A., in press. The role of slip length and precipitation on the ductility and fracture behavior of isotropic Al–Li–Cu–X alloys, Recent Advances in Non-Ferrous Metals Processing Symposium.

Duva, J.M., Daeubler, M.A., Starke Jr., E.A., Luetjering, G., 1988. Large shearable particles lead to coarse slip in particle reinforced alloys. Acta Metall. 36, 585.

Furukawa, M., Miura, Y., Nemoto, M., 1985. Strengthening mechanisms in Al–Li alloys containing coherent ordered particles. Trans. Japan Inst. Metals 26, 230.

Gable, B.M., Zhu, A.W., Csontos, A.A., Starke Jr., E.A., 2001. The role of plastic deformation on the competitive microstructural evolution and mechanical properties of a novel Al–Li–Cu–X alloy. Journal of Light Metals 1 (1), 1–14.

Gregson, P.J., Flower, H.M., 1985. Microstructural control of toughness in aluminium–lithium alloys. Acta Metall. 33, 527.

Gysler, A., Terlinde, G., Lutjering, G., 1976. Influence of grain size on the ductility of age-hardened titanium alloys. In: Proceedings of the Third International Conference on Titanium. Plenum Press, New York, p. 1931.

Hardy, H.K., Silcock, J.M., 1959. J. Inst. Metals 84, 423.

Hornbogen, E., 1975. Grain-size dependence of the fracture toughness of precipitation-hardened alloys. Z. Metallk 66, 511.

Howe, J.M., Lee, J., Vasudevan, A.K., 1988. Structure and deformation behavior of T sub 1 precipitate plates in an Al–2Li–1Cu alloy. Metall. Trans. A 19A, 2911.

Hopkins, A.K., Jata, K.V., Rioja, R.J., 1996. The anisotropy and texture of Al–Li alloys. In: Aluminum Alloys, Their Physical and Mechanical Properties – Proceedings ICAA5. In: Driver, J.H., Dubost, B.,

Durand, E.A. Jr., Fougeres, R., Guyot, P., Sainfort, P., Suery, M. (Eds.), 1989, Materials Science Forum, 217–222. Transtec Publications.

Huang, J.C., Ardell, A., 1988. Addition rules and the contribution of δ' precipitates to strengthening of aged Al–Li–Cu alloys. Acta. Metall. 36, 2995.

Jata, K.V., Starke Jr., E.A., 1986. Fatigue crack growth and fracture toughness behavior of an Al–Li–Cu alloy. Metall. Trans. A. 17A, 1011.

Jata, K.V., Vasudevan, A.K., 1998. Effect of fabrication and microstructure on the fracture initiation and growth toughness of Al–Li–Cu alloys. Mater. Sci. Eng. A 241, 104.

Jata, K.V., Hopkins, A.K., Rioja, R.J., 1996. The anisotropy and texture of Al–Li alloys. Materials Science Forum 217–222, 647–652.

Kuo, V.W., Starke Jr., E.A., 1985. The development of two texture variants and their effect on the mechanical behavior of a high strength P/M aluminum alloy, X7091. Metall. Trans A 16A, 1089.

Lewis, R.E, Starke Jr., E.A, Coons, W.C., Shiflet, G.J., Willner, E., Bjeletich, J.G., Mills, C.H., Harrington, R.M., Petrakis, D.N., 1987. Microstructure and properties of Al–Li–Cu–Mg–Zr (8090) heavy section forgings. Al–Li Alloys IVLes Editions de Phsique C3, 643.

Lutjering, G., Weissmann, S., 1970. Mechanical properties of age-hardenable Ti–Al alloys. Acta Metall. 18, 785.

Martin, J.W., 1979. Micromechanisms in Particle-hardened Alloys. Cambridge University Press, Cambridge.

Mendiratta, M.G., Sastry, S.M., Smith, J.V., 1976. Effect of grain size upon flow and fracture in a precipitation-strengthened Ti–8 wt% Al–0.25 wt% Si alloy. J. Mater. Sci. 11, 1835.

Miura, S., Hamashima, K., Aust, K.T., 1980. Plastic deformation of aluminium bicrystals having sigma-7 and sigma-21 coincidence tilt boundaries. Acta Metall. 28, 1591.

Miura, S., Saeki, Y., 1977. Plastic deformation and prominent cross slip of 100 oriented al single crystals. Trans. Jpn. Inst. Met. 18, 843.

Miura, S., Saeki, Y., 1978. Plastic deformation of Al bicrystals 100 oriented. Acta Metall. 26, 93.

Nie, J.F., Muddle, B.C., Polmear, I.J., 1996. The effect of precipitate shape and orientation on dispersion strengthening in high strength aluminium alloys. Mater. Sci. Forum 217–222, 1257.

Noble, B., Thompson, G.E., 1972. T_1 (Altextsubscript2CuLi) precipitation in Al–Cu–Li alloys. Metal Sci. J. 6, 167.

Roven, H.J., 1992. A model for fracture toughness predictions in aluminium alloys exhibiting band decohesion mechanism. Scripta Metall. Mater. 26, 1383.

Sanders Jr., T.H., Starke Jr., E.A., 1982. The effect of slip distribution on the monotonic and cyclic ductility of Al–Li binary alloy. Acta Metall. 30, 927.

Sugamata, M., Blankenship Jr., C.P., Starke Jr., E.A., 1993. Predicting plane strain fracture toughness of Al–Li–Cu–Mg alloys. Mater. Sci. Eng. A163, 1.

Terlinde, G., Luetjering, G., 1982. Influence of grain size and age-hardening on dislocation pile-ups and tensile fracture for a Ti–Al alloy. Metall. Trans. A 13A, 1283.

Walsh, J.A., Jata, K.V., Starke Jr., E.A., 1989. The influence of manganese dispersoid content and stress state on ductile fracture of 2134 type aluminum alloys. Acta Metall. 37, 2861.